

Gravitational-wave sensitivity curves

C J Moore¹, C P L Berry^{1,2} & R H Cole¹

¹ Institute of Astronomy, Madingley Road, Cambridge, CB3 0HA, United Kingdom

² School of Physics and Astronomy, University of Birmingham, Edgbaston, Birmingham B15 2TT, United Kingdom

E-mail: cjm96@ast.cam.ac.uk

Abstract. There are several common conventions use by the gravitational wave community to describe the amplitude of sources and the sensitivity of detectors. These are frequently confused. We outline the merits of and differences between the various quantities used for parameterizing noise curves and characterizing gravitational wave amplitudes. We conclude by producing plots that consistently compare different detectors. Similar figures can be generated on-line for general use at <http://www.ast.cam.ac.uk/~rhc26/sources/>.

PACS numbers: 04.30.-w, 04.30.Db, 04.80.Nn, 95.55.Ym

1. Introduction

The next few years promises to deliver the first direct detection of gravitational waves (GWs). This will most likely be achieved by the advanced LIGO (Harry & LIGO Scientific Collaboration, 2010) and Virgo (Accadia et al., 2011) detectors operating in the frequency range $(10\text{--}10^3)$ Hz. By the end of the decade, it is expected that pulsar timing arrays (Foster & Backer, 1990) shall detect very low frequency GWs around 10^{-8} Hz. Further into the future, space-based detectors, such as eLISA (Amaro-Seoane et al., 2012b), will probe GWs in the millihertz regime. This shall herald the beginning of multi-wavelength GW astronomy.

There already exists an extensive literature assessing the potential of all of these detectors to probe the astrophysics of various sources. There are several different methods commonly used to describe the sensitivity of a GW detector and the strength of a GW source. It is common practice in GW astronomy to summarise this information on a sensitivity curve plot. When producing these plots, it is desirable to have a consistent convention between detectors and sources which allows information about both to be plotted on the same graph. Ideally, the detectors and sources are represented in such a way that the relative detectability of the signals is immediately apparent from the plot.

In this work we discuss the differing conventions commonly used in sensitivity curve plots. The amplitude of a GW is a strain, a dimensionless quantity h . This gives a fractional change in length, or equivalently light travel time, across a detector. The strain is small, making it a challenge to measure. To calibrate our expectations for detection it is necessary to quantify the sensitivity of our instruments and the strength of the target signals. There are three commonly used descriptions: the characteristic strain, the power spectral density and the spectral energy density. We aim to disambiguate these three and give a concrete comparison of different detectors. It is hoped that this will provide a useful reference for new and experienced researchers in this field alike.

We begin by expounding the various conventions and the relationships between the conventions in sections 2 and 3. A review of GW detectors (both current and proposed) is given in section 4 and a review of GW sources is given in section 5. In Appendix A several example sensitivity curves are presented. A website where similar figures can be generated is available at www.ast.cam.ac.uk/~rhc26/sources/. Here the user may select which sources and detectors to include to tailor the figure to their specific requirements.

2. Signal analysis

Gravitational radiation has two independent polarization states denoted $+$ and \times ; a general signal can be described as a linear combination of the two polarization states, $h = A_+h_+ + A_\times h_\times$. The sensitivity of a detector to each of these depends upon the relative orientations of the source and detector. The output of a gravitational wave detector, $s(t)$, will contain a superposition of noise, $n(t)$, and possibly a signal, $h(t)$,

$$s(t) = n(t) + h(t) . \quad (1)$$

It will be necessary to work with the Fourier transform of the signal, the most common convention used in the GW community is

$$\begin{aligned} x(t) &= \mathcal{F}^{-1} \{ \tilde{x}(f) \} = \int_{-\infty}^{\infty} df \tilde{x}(f) \exp(2\pi i f t) \\ \tilde{x}(f) &= \mathcal{F} \{ x(t) \} = \int_{-\infty}^{\infty} dt x(t) \exp(-2\pi i f t) . \end{aligned} \quad (2)$$

For simplicity it is assumed that the noise in the GW detector is stationary and Gaussian (with zero mean), under these assumptions the noise is fully characterised via the *one-sided* noise power spectral density, $S_n(f)$,[‡],

$$\langle \tilde{n}(f) \tilde{n}^*(f') \rangle = \frac{1}{2} \delta(f - f') S_n(f) . \quad (3)$$

[‡] An alternative convention is to use the two-sided power spectral density $S_n^{(2)}(f) = S_n(f)/2$.

Angled brackets $\langle \dots \rangle$ denote an ensemble average over many realisations of the noise. In reality we have only a single system to work with, so the ensemble average is replaced by a time average. The procedure is to measure the noise over a sufficiently long duration, T , and then compute the Fourier transform, $\tilde{n}(f)$, with a frequency resolution $\Delta f = T^{-1}$. This is then repeated many times to give the ensemble average; this procedure assumes the system is ergodic. Since the GW signal and detector output are real it follows that $\tilde{h}(-f) = \tilde{h}^*(f)$ and $\tilde{n}(-f) = \tilde{n}^*(f)$; therefore, $S_n(f) = S_n(-f)$. The fact $S_n(f)$ is an even function means that Fourier integrals over all frequencies can instead be written as integrals over positive frequencies only (see, for example, equations (6) and (11)), it is for this reason that $S_n(f)$ is called the *one-sided* power spectral density. It is straightforward to show that the power spectral density has the property that integrated over all positive frequencies it gives the mean square noise amplitude in the detector.

$$\begin{aligned} \overline{n(t)^2} &= \lim_{T \rightarrow \infty} \frac{1}{2T} \int_{-T}^T dt |n(t)|^2 \\ &= \lim_{T \rightarrow \infty} \frac{1}{2T} \int_{-T}^T dt \int_{-\infty}^{\infty} df \int_{-\infty}^{\infty} df' \tilde{n}(f) \tilde{n}^*(f') \exp(2\pi i(f - f')t) \end{aligned} \quad (4)$$

Using the property of Fourier transforms, $\mathcal{F}\{n(t + \tau)\}(f) = \tilde{n}(f) \exp(-2\pi i f \tau)$, the exponential factors in equation (4) may be absorbed as a time translation of the noise by an amount t . The noise is stationary and so its long term time average is invariant under this time translation and is given by Equation (3).

$$\begin{aligned} \overline{n(t)^2} &= \lim_{T \rightarrow \infty} \frac{1}{2T} \int_{-T}^T \int_{-\infty}^{\infty} df \int_{-\infty}^{\infty} df' \mathcal{F}\{n(\tau - t)\}(f) \mathcal{F}\{n(\tau - t)\}(f')^* \\ &= \int_{-\infty}^{\infty} df \int_{-\infty}^{\infty} df' \langle \tilde{n}(f) \tilde{n}^*(f') \rangle \\ &= \int_0^{\infty} df S_n(f) \end{aligned} \quad (5)$$

Using the property of Fourier transforms, $\mathcal{F}\{n(t + \tau)\}(f) = \tilde{n}(f) \exp(-2\pi i f \tau)$, the time average can be turned into an ensemble average and hence the definition of power spectral density in (3) may be used.

$$\begin{aligned} \overline{n(t)^2} &= \lim_{T \rightarrow \infty} \frac{1}{2T} \int_{-\infty}^{\infty} df \int_{-\infty}^{\infty} df' \int_{-T}^T dt \tilde{n}(f) \tilde{n}^*(f') \\ &= \int_{-\infty}^{\infty} df \int_{-\infty}^{\infty} df' \langle \tilde{n}(f) \tilde{n}^*(f') \rangle \\ &= \int_0^{\infty} df S_n(f) \end{aligned} \quad (6)$$

Given a detector output the challenge is to extract the signal. There is a well known solution to this problem which involves constructing a Wiener optimal filter. Let $K(t)$ be the filter

function with Fourier transform $\tilde{K}(f)$. Convolving this with the detector output gives a contribution from the signal and a contribution from the noise

$$(s * K)(\tau) = \int_{-\infty}^{\infty} dt (n(t) + h(t))K(t - \tau) = S + N. \quad (7)$$

The signal contribution, S , is defined as the expectation of the convolution in (7) when a signal is present, maximised by varying the offset τ . Since the expectation of pure noise is zero it follows that

$$S = \int_{-\infty}^{\infty} dt h(t)K(t) = \int_{-\infty}^{\infty} dt h(t)K^*(t) = \int_{-\infty}^{\infty} df \tilde{h}(f)\tilde{K}^*(f). \quad (8)$$

The squared contribution from noise, N^2 , is defined as the mean square of the convolution in (7) when no signal is present,

$$\begin{aligned} N^2 &= \int_{-\infty}^{\infty} dt \int_{-\infty}^{\infty} dt' K(t)K(t') \langle n(t)n(t') \rangle \\ &= \int_{-\infty}^{\infty} dt \int_{-\infty}^{\infty} dt' K(t)K^*(t') \int_{-\infty}^{\infty} df \int_{-\infty}^{\infty} df' \langle \tilde{n}(f)\tilde{n}^*(f') \rangle \exp(2\pi i(ft - f't')) \\ &= \int_{-\infty}^{\infty} df \frac{1}{2} S_n(f) \tilde{K}(f) \tilde{K}^*(f), \end{aligned} \quad (9)$$

where the definition of $S_n(f)$ from (3) has been used. Hence the optimum signal-to-noise ratio (SNR), ϱ , is given by

$$\varrho^2 = \frac{(S)^2}{N^2} = \frac{\left(\frac{1}{2} S_n(f) \tilde{K}(f) \middle| \tilde{h} \right)^2}{\left(\frac{1}{2} S_n(f) \tilde{K}(f) \middle| \frac{1}{2} S_n(f) \tilde{K}(f) \right)}, \quad (10)$$

where the inner product between a pair of signals A and B has been defined

$$(A|B) = 4\Re \left\{ \int_0^{\infty} df \frac{\tilde{A}^*(f)\tilde{B}(f)}{S_n(f)} \right\}. \quad (11)$$

The optimum filter is that which maximises the SNR in (10). From the Cauchy-Schwarz inequality it follows that the optimum filter is

$$\tilde{K}(f) = \frac{\tilde{h}(f)}{S_n(f)}. \quad (12)$$

This is the Wiener filter, it may be multiplied by an arbitrary constant since this will not change the SNR. Notice that in order to construct the Wiener filter it is necessary to know *a priori* the form of the signal, $\tilde{h}(f)$. It is common to define the noise amplitude and characteristic strain as

$$h_n(f)^2 = f S_n(f) \quad (13)$$

$$h_c(f)^2 = 4f^2 \left| \tilde{h}(f) \right|^2, \quad (14)$$

so that the SNR in (10) may be written compactly as

$$\varrho^2 = \int_0^\infty d(\log f) \left(\frac{h_c(f)}{h_n(f)} \right)^2. \quad (15)$$

The strain amplitudes $h_n(f)$ and $h_c(f)$ are dimensionless, while $S_n(f)$ has units of inverse frequency.

Whilst the magnitude of the Fourier transform of the signal, $h(f) = |\tilde{h}(f)|$, provides a simple quantification of the GW amplitude as a function of frequency it has one main deficiency. For an inspiralling source the instantaneous amplitude can be orders of magnitude below the noise level in the detector; however, as the signal continues over many orbits the SNR can be integrated up to a detectable level. It is desirable to have a quantification of the GW amplitude that accounts for this effect; three such methods are described in the following sections.

2.1. Characteristic strain

One sensible choice of quantities to plot on a sensitivity curve is h_n for the detector and h_c for the source (see figure A1). Using this convention, when plotting on a log-log scale, the area between the source and detector curves is related to the SNR via (15). This convention allows the reader to “integrate by eye” for a given detector to assess the detectability of a given source. Also, when using this convention the reader does not need to worry about the observation time for each source because this is already accounted for in the definition of characteristic strain. An additional advantage of this convention is that the values on the strain axis for the detector curve have a simple physical interpretation, they correspond to the root-mean-square noise in a bandwidth f . One downside to plotting characteristic strain is that the values on the strain axis do not directly relate to the amplitude of the waves from the source. Another disadvantage is that the characteristic strain for a monochromatic source is infinite!

2.2. Power spectral density

Another common quantity to plot on sensitivity curves is the square root of the power spectral density (see figure A2), which from (13) is given by

$$\sqrt{S_n(f)} = h_n(f) f^{-1/2} \quad \text{for detectors, and by analogy} \quad (16)$$

$$\sqrt{S_h(f)} = h_c(f) f^{-1/2} \quad \text{for sources.} \quad (17)$$

The power spectral density is the most commonly plotted quantity in sensitivity curves in the literature and it has the nice property, proven in equation (6), that integrated over all positive frequencies it gives the mean square amplitude of the signal in the detector.

2.3. Energy density

A third way of describing the detectability of a GW is through the energy carried by the waves, this quantity has the obvious advantage of having a clear physical significance. This quantity is most commonly used in sensitivity curves showing stochastic backgrounds of GWs, see section 3.2. The energy in GWs is described by the Isaacson stress tensor (Misner et al., 1973)

$$T_{\mu\nu} = \frac{c^2}{32\pi G} \langle \partial_\mu \bar{h}_{\alpha\beta} \partial_\nu \bar{h}^{\alpha\beta} \rangle . \quad (18)$$

The energy density, ρc^2 , is given by the T_{00} component of this tensor. Using this together with (3) to calculate the energy density in the GW signal gives

$$\rho c^2 = \frac{c^2}{16\pi G} \int_{-\infty}^{\infty} df (2\pi f)^2 \tilde{h}(f) \tilde{h}^*(f) = \int_0^{\infty} df \frac{\pi c^2}{4G} f^2 S_h(f) , \quad (19)$$

where the definitions (17) and (14) have been used. Equation (19) motivates the definition of the spectral energy density in GWs, S_E , the energy per unit volume of space, per unit frequency, Hellings & Downs (1983)

$$S_E(f) = \frac{\pi c^2}{4G} f^2 S_h(f) , \quad (20)$$

and a corresponding expression for the noise with $S_n(f)$. It is usual to define the dimensionless quantity Ω_{GW} as the energy density per logarithmic frequency interval normalised to the critical density of the universe

$$\Omega_{\text{GW}}(f) = \frac{f S_E(f)}{\rho_c c^2} . \quad (21)$$

The critical density of the universe is $\rho_c = 3H_0^2/8\pi G$, where $H_0 = h_{100} \times 100 \text{ km s}^{-1} \text{ Mpc}^{-1}$ is the Hubble constant (this equation serves as a definition of h_{100} , which here has nothing to do with strain). The most common quantity related to energy density to be plotted on sensitivity curves is $\Omega_{\text{GW}} h_{100}^2$ (figure A3). This quantity has one aesthetic advantage over the others: it accounts for the fact that there is less energy in low frequency waves of the same amplitude and does not place the sensitivity curves of very low frequency detectors much higher than most ground based detectors.

2.4. Relating the different descriptions

The dimensionless energy density in GWs, Ω_{GW} , the spectral energy density in GWs, S_E , the one-sided power spectral density, S_h , and the characteristic strain are all related via

$$\Omega_{\text{GW}}(f) = \frac{f S_E(f)}{\rho_c c^2} = \frac{\pi}{4G\rho_c} f^2 h_c(f)^2 = \frac{\pi}{4G\rho_c} f^3 S_h(f) , \quad (22)$$

and corresponding expressions for the noise with $S_n(f)$ and $h_n(f)$.

3. Types of source

Sources of GWs can be broadly split into three categories: well modelled sources, for which we have a description of the expected waveform; stochastic backgrounds, for which we can describe the statistical behaviour; and unmodelled (or poorly-modelled) transient sources. The classic example of a well modelled source is the inspiral of two compact objects, this is discussed in section 3.1. Stochastic backgrounds can either be formed from many overlapping sources, which are each individually susceptible to being modelled, or from some intrinsically random process, these are discussed in section 3.2. An example of an unmodelled (or poorly-modelled) transient source is a supernova; searches of this type are often called burst searches and are discussed in section 3.3.

3.1. Inspirals

Inspiralling binaries spend a variable amount of time in each frequency band. If ϕ is the orbital phase then the number of cycles generated at frequency f can be estimated as

$$\mathcal{N}_{\text{cycles}} = \frac{f}{2\pi} \frac{d\phi}{df} = \frac{f^2}{\dot{f}}, \quad (23)$$

where an overdot represents the time derivative and $f = \dot{\phi}$. The squared SNR will scale with $\mathcal{N}_{\text{cycles}}$, so it would be expected that $h_c(f) \approx \sqrt{\mathcal{N}_{\text{cycles}}} \tilde{h}(f)$. The exact conversion can be derived by considering the Fourier transform in the stationary phase approximation. Consider a source signal with approximately constant amplitude, h , and central frequency f' .

$$h(t) = h \exp(i\phi(t)) \quad (24)$$

$$\Rightarrow \tilde{h}(f) = \int_{-\infty}^{\infty} dt h \exp\left(2\pi i \left(\frac{\phi(t)}{2\pi t} - f\right) t\right) \quad (25)$$

Without loss of generality assume an initial phase of zero and expand the exponent in powers of t ,

$$\begin{aligned} \tilde{h}(f) &\approx \int_{-\infty}^{\infty} dt h \exp\left[2\pi i \dot{f}' \left(t^2 + \frac{f' - f}{\dot{f}'} t\right)\right] \\ &\approx h \exp\left[-\pi i \frac{(f' - f)^2}{2\dot{f}'}\right] \int_{-\infty}^{\infty} dt \exp\left[2\pi i \dot{f}' \left(t + \frac{f' - f}{2\dot{f}'}\right)^2\right] \\ &\approx \frac{h}{\sqrt{2i\dot{f}'}} \exp\left[-\pi i \frac{(f' - f)^2}{2\dot{f}'}\right]. \end{aligned} \quad (26)$$

From (13) and (26) the characteristic strain and the Fourier transform can be related for inspiralling sources (Finn & Thorne, 2000)

$$h_c(f) = \sqrt{\frac{2f^2}{\dot{f}}} h. \quad (27)$$

Equation (27) is the relation between $h_c(f)$ and the instantaneous amplitude h for an inspiralling source; for other types of source a new relation which satisfies (15) will have to be found. Equation (15) should be considered as the definition of characteristic strain and (27) a consequence of it for inspirals.

3.2. Stochastic backgrounds

Another important source of GWs arises from stochastic backgrounds due to large populations of individually unresolvable sources. The population of sources will in general be at cosmological distances and it is necessary to distinguish the frequency in the source rest frame, f_r , from the measured frequency, f ; these are related through the redshift, z , via $f_r = (1+z)f$. The comoving number density of sources, n , producing the background will also be a function of redshift; if the sources producing the stochastic background are all in the local universe then simply set $n(z) = \delta(z)$ and replace $d_L(z)$ with d in all that follows (where $d_L(z)$ and d are respectively the luminosity and comoving distances to the source, $d_L(z) = (1+z)d_m$). Equation (22) gives an expression for the energy density in GWs per logarithmic frequency interval,

$$f S_E(f) = \frac{\pi c^2}{4G} f^2 h_c(f)^2. \quad (28)$$

The total energy emitted in the logarithmic frequency interval $d(\log(f_r))$ by a single binary in the population is $(dE_{\text{GW}}/d(\log f_r)) d(\log f_r)$; the energy density may be written as

$$f S_E(f) = \int_0^\infty dz \frac{dn}{dz} \frac{1}{(1+z)} \frac{1}{d_L(z)^2} \frac{dE_{\text{GW}}}{d(\log f_r)}, \quad (29)$$

where the factor of $(1+z)^{-1}$ accounts for the redshift of the energy.

For simplicity consider all the binaries comprising the background to be in circular orbits with frequencies $\nu = f_r/2$, and to be far from their last stable orbit; the energy radiated may then be calculated using the quadrupole approximation, Peters & Mathews (1963). The chirp mass is defined as $\mathcal{M} = \mu^{3/5} M^{2/5}$, where μ is the reduced mass and M is the total mass of the binary. The number density of sources will also be a function of chirp mass, $n(z, \mathcal{M})$. The energy in GWs from a single binary per logarithmic frequency interval is,

$$\frac{dE_{\text{GW}}}{d(\log f_r)} = \frac{G^{2/3} \pi^{2/3}}{3} \mathcal{M}^{5/3} f_r^{2/3}, \quad (30)$$

between an minimum and maximum frequency set by the initial and final radius of the binary orbit. Here we assume that the maximum and minimum frequencies are outside of the range of frequencies probed by our detector and hence may be neglected. Using (28), (29) and (30) an expression for characteristic strain can now be found, Sesana et al. (2008)

$$h_c(f)^2 = \frac{4G^{5/3}}{3\pi^{1/3}c^2} f^{-4/3} \int_0^\infty dz \int_0^\infty d\mathcal{M} \frac{d^2n}{dz d\mathcal{M}} \frac{1}{d_L(z)^2} \left(\frac{\mathcal{M}^5}{1+z} \right)^{1/3}. \quad (31)$$

From (31) it can be seen that the characteristic strain due to a stochastic background of binaries is a power law in frequency with spectral index $\alpha = -2/3$. The amplitude of the background depends on the population statistics of the binaries under consideration via $n(z, \mathcal{M})$. The power law is often parametrised as

$$h_c(f) = A \left(\frac{f}{f_0} \right)^\alpha, \quad (32)$$

and constraints are then placed on A . In practice this power law will also have upper and lower frequency cut-offs related to the population of objects creating the GW spectrum. The stochastic background due to other sources, such as cosmic strings or relic GWs from the early Universe, can also be written in the same form as (32) but with different spectral indices: $\alpha = -7/6$ for cosmic strings or α in the range -1 to -0.8 for relic GWs, Jenet et al. (2006).

3.3. Burst sources

Some sources of GWs can produce signals with large amplitudes, greater than the detector noise. The duration of such a signal is typically very short, of the order of a few wave periods, and so there is not time to accumulate SNR in each frequency band in the way inspirals do. As a consequence, waveform models are not required to produce a detection; we simply rely on the "excess power" produced by these so-called burst sources. Typically, we may be looking for signals from core collapse supernovae (Ott, 2009), the late stages of merging compact binaries, or more generally, signals from any unexpected or poorly modelled sources.

Burst searches are often carried out using time-frequency techniques. The data stream from a detector is temporally split into segments, the length of which can be tuned to give greater sensitivity to particular sources. Each segment is then transformed into the frequency domain, whitened and normalised to the noise spectrum to produce a time-frequency plot. Potential GW signals are identified by searching for clusters of pixels that contain an excess of power (see e.g. Abadie et al. (2012a)).

The presence of excess power across a number of pixels eliminates modelled noise sources, but such a cluster may also be caused by atypical noise within a detector. We can improve our confidence of a GW signal by making use of information obtained from other GW

detectors. Signals across a network of detectors should have compatible arrival times (given the sky direction) as well as consistent amplitudes, frequencies and shapes of the waveform. Different pipelines are currently in use that analyse the signal consistency in different ways: both coincidence searches (Chatterji et al., 2004) and fully coherent methods (Klimenko et al., 2008) are used.

An important aspect of burst search algorithms is to accurately estimate the noise properties within each time segment. To this extent, null data streams can be constructed that should be insensitive to real GW signals. In order to estimate the false alarm rate, the data from different detectors can be shifted in time to remove any genuine coincident GW signals. These time-shifts are then analysed to simulate the potential occurrence of coincident noise events. The algorithms are tuned using time-shifted data to ensure there is no bias in the final search.

As discussed in 3.1, the expected relation between $h_c(f)$ and a typical waveform $\tilde{h}(f)$ is simply

$$h_c(f) = \tilde{h}(f) \sqrt{\mathcal{N}_{\text{cycles}}} , \quad (33)$$

where $\mathcal{N}_{\text{cycles}}$ is the number of cycles of radiation generated by the source. Here, $\mathcal{N}_{\text{cycles}}$ is of order unity and $\tilde{h}(f)$ is strongly peaked around some central frequency.

4. Detectors

4.1. Operating principle of an interferometric detector

All of the man-made detectors discussed in this section work on the principle of interferometry. Such detectors work by taking a beam of monochromatic light and splitting it into two beams travelling at some angle to each other. Each beam is passed in to a Fabry-Pérot cavity where it undergoes a number of round trips before being recombined to form an interference pattern. The ends of the cavity are, in the ideal case, freely floating test masses which move in response to a passing GW, this effect is measured by observing the changing interference pattern.

The response of a detector to an incident plane fronted GW depends upon the relative orientations of the detector and the incoming wave. Choose the origin of our coordinate system to be the beam-splitter of the interferometer and let l_1^i and l_2^i be unit 3-vectors pointing along the two arms. In the absence of noise the output of the detector is the difference in strain between the two arms (Misner et al., 1973)

$$h(t) = \frac{1}{2} h_{ij} (l_1^i l_1^j - l_2^i l_2^j) , \quad (34)$$

where h_{ij} are the spatial components of the GW metric perturbation. Let n^i be the unit 3-vector pointing towards the source of the GWs, with spherical polar angles (θ, ϕ) relative

to some axes fixed to the detector, also let p^i and q^i be unit vectors orthogonal to n^i . There remains a freedom in the coordinates described, a rotation of p^i and q^i through an angle ψ about n^i . Define the basis tensors,

$$\begin{aligned} H_{ij}^+ &= p_i p_j - q_i q_j \\ H_{ij}^\times &= p_i q_j + q_i p_j . \end{aligned} \quad (35)$$

Consider a single frequency component of the incident GW, the strain induced by the incident GW may be written as

$$h_{ij} = A_+ H_{ij}^+ \cos(2\pi f t) + A_\times H_{ij}^\times \cos(2\pi f t + \Delta\phi) , \quad (36)$$

where A_+ and A_\times are the amplitudes of the two polarisation states. Combining (34) and (36) allows the detector output to be written as

$$h(t) = F^+(\theta, \phi, \psi) A_+ \cos(2\pi f t) + F^\times(\theta, \phi, \psi) A_\times \cos(2\pi f t + \Delta\phi) , \quad (37)$$

where the response functions inherit their angular dependence from the choice of coordinates,

$$\begin{aligned} F^+(\theta, \phi, \psi) &= \frac{1}{2} H_{ij}^+ (l_1^i l_1^j - l_2^i l_2^j) \\ F^\times(\theta, \phi, \psi) &= \frac{1}{2} H_{ij}^\times (l_1^i l_1^j - l_2^i l_2^j) . \end{aligned} \quad (38)$$

The response function of a two-arm interferometric detector is quadrupolar, an example is plotted in figure 1.

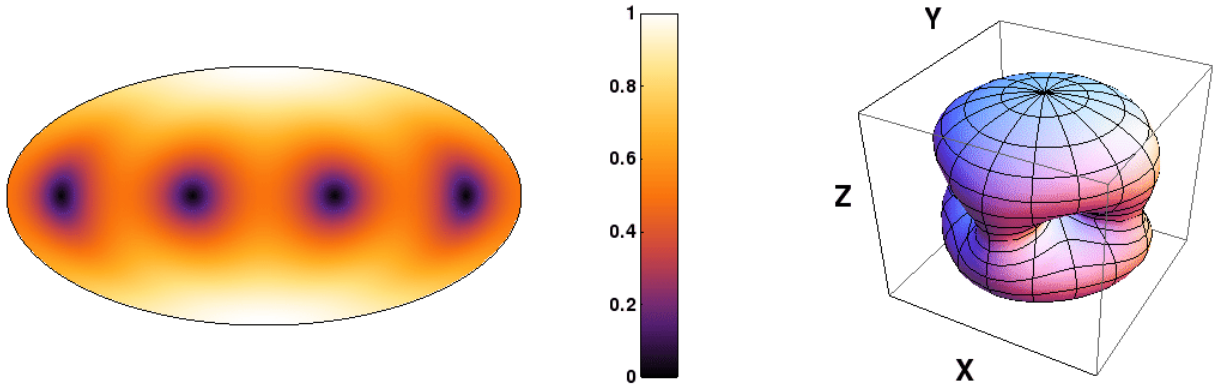


Figure 1: The angular response function of an interferometric detector shown both as a surface plot and in an Aitoff-Hammer projection. The two detector arms lie in the xy plane either side of one of the zeros in the response.

Throughout this paper detector sensitivity refers to the polarisation and sky averaged sensitivity, F , where

$$F^2 = \int_0^{2\pi} \frac{d\psi}{2\pi} \int_0^\pi \int_0^{2\pi} \frac{\sin\theta d\theta d\phi}{4\pi} \left(\frac{F^+(\theta, \phi, \psi)^2 + F^\times(\theta, \phi, \psi)^2}{2} \right). \quad (39)$$

For a single 90° interferometer, such as LIGO (Laser Interferometer GW Observatory), the sky and polarisation averaged response is $F = \sqrt{1/5} \approx 0.447$.

A detector may consist of several interferometers. Let F_a be the averaged response of the a^{th} interferometer. The average response of the detector network is obtained by adding in quadrature,

$$F_{\text{Total}}^2 = \frac{1}{(\text{Number of interferometers})} \sum_{x=1}^N F_x^2. \quad (40)$$

The averaging in (39) assumes a uniform distribution of polarisation angles ψ . This will be the case for a stochastic background, however for a non-inspiralling circular binary the polarisation will be a function of the two spherical polar angles (ι, ξ) specifying the orientation of the binary's orbital angular momentum. Here ι is the polar angle between the orbital angular momentum and the line joining the source to the detector while ξ is the azimuthal angle around the same line. In this case the correct average to characterise the detector sensitivity would be an average over all four angles $(\theta, \phi, \iota, \xi)$. If the binary is inspiralling then the polarisation will depend on still more parameters which need to be averaged over. These more complicated averages all have the property that they depend on both the detector and the source, hence they are unhelpful for our present purpose. In addition the different averages don't work out to be so different from each other; Finn & Chernoff (1993) calculated the sensitivity for a detector with the LIGO geometry averaged over the four angles $(\theta, \phi, \iota, \xi)$ as $\sqrt{4/25} = 0.4$ times peak sensitivity, which should be compared with the value $\sqrt{1/5} \approx 0.447$ above. For the remainder of this paper the 3 angle average defined in (39) will be used.

4.2. Ground based detectors

On Earth approximations to the free floating test masses described above are achieved by suspending the mass from a pendulum system with natural frequency much greater than that of the GW. The interferometric detectors listed in Table 1 are all sensitive to GWs in the frequency range $\mathcal{O}(10 - 10^3)$ Hz. They all have multiple narrow lines in their sensitivity curves, which arise from noise sources in the instrument including resonances in the suspension system and electronic noise at multiples of 60 Hz: these have been removed in figures A1, A2 and A3 for clarity. The detectors fall broadly into three categories: 1st generation detectors, which have already operated; 2nd generation detectors currently under construction; and 3rd generation detectors at the planning stage.

Table 1: For the aVIRGO sensitivity curve an interpolation to the data published on <https://wwwcascina.virgo.infn.it/advirgo/> (2013) was used. For KAGRA (Kamioka Gravitational Wave Detector) an interpolation to the data for version D of the detector published on <http://gwcenter.icrr.u-tokyo.ac.jp/en/researcher/parameter> (2013) was used. For the remaining detectors analytic fits to the sensitivity curves due to Sathyaprakash & Schutz (2009) were used.

Detector	Country	Arm length	Approximate date	Generation
GEO600 ^a	Germany	600 m	2001-present	1 st
TAMA300 ^b	Japan	300 m	1995-present	1 st
iLIGO ^c	US	4 km	2004-2010	1 st
iVIRGO ^d	Italy	3 km	2007-2010	1 st
aLIGO ^e	US	4 km	<i>est.</i> 2016	2 nd
KAGRA ^f	Japan	3 km	<i>est.</i> 2018	2 nd
aVIRGO ^g	Italy	3 km	<i>est.</i> 2017	2 nd
ET (Einstein Telescope) ^h	Italy	10 km	<i>est.</i> 2025	3 rd

^aGrote & LIGO Scientific Collaboration (2008), ^bAndo & TAMA Collaboration (2002),
^cAbbott et al. (2009), ^dAccadia et al. (2012), ^eHarry & LIGO Scientific Collaboration (2010),
^fSomiya (2012), ^gAcernese et al. (2009), ^hHild et al. (2011).

4.3. Space based detectors

Space based detectors work on similar principles to ground based detectors but with the test masses residing inside of independent, widely separated satellites. Space based detectors are sensitive to lower frequency GWs than their ground based counterparts, this is partly because space based detectors can have much longer arms and partly because they are unaffected by seismic noise which limits the low frequency performance of ground based detectors.

The canonical design for a space based detector is LISA (Laser Interferometer Space Antenna), which would be sensitive to milli-Hz GWs. LISA would consist of three satellites flying in a triangular constellation with arms of length 5×10^9 m in a 1 AU orbit around the sun, trailing the Earth by 20° . The laser arms in a LISA like detector are not a Fabry-Pérot cavity, the light only travels once along each arm. All of the sources discussed here lie within LISA’s sensitivity reach. eLISA (evolved LISA) is a simpler version of LISA designed to probe the same frequency range, while proposals such as ALIA (Advanced Laser Interferometer Antenna), BBO (Big Bang Observer) and DECIGO (DECI-Hertz Interferometer GW Observatory) are designed to probe deci-Hz GWs.

4.3.1. LISA and eLISA We use an analytic fit to the instrumental noise curve given by Sathyaprakash & Schutz (2009). When observing individual sources with LISA there is an

additional contribution to the noise from a background of unresolvable binaries. This is not included here as we consider the background as a source of GWs, see section 5.2.2. eLISA is a re-scoped version of the classic LISA mission, the main differences are shorter arms (10^9 m instead of 5×10^9 m), two laser arms instead of three and a different orbit (drifting away from Earth instead of 20° Earth trailing). The effect of these changes is a slightly reduced peak sensitivity and a shift to higher frequencies. We use an analytic fit to the instrumental noise curve given by Amaro-Seoane et al. (2012a).

4.3.2. ALIA, DECIGO and BBO These missions are designed to probe the deci-Hz region of the GW spectrum, they are considerably more ambitious than the LISA or eLISA mission and their launches will be further into the future. For ALIA a simple analytic fit to the sensitivity curve is used, while for DECIGO and BBO fits to the sensitivity curves given by Yagi & Seto (2011) are used.

4.4. Pulsar timing arrays (PTAs)

PTAs can be thought of as naturally occurring interferometers with galactic scale arm lengths, hence they are sensitive to much lower frequencies than the detectors considered so far. Each pulsar is a very regular clock and the measured pulse arrival time (in practice, arrival times are corrected to arrival times at the solar-system barycenter, SSB) can be compared against a prediction leaving a residual which includes the effects of passing GWs. Using an array of these pulsars spread across the sky allows us to correlate residuals between different pulsars and exploit the fact that the GWs influence all pulsars where as intrinsic pulsar noise clearly does not. The correlation between different pulsars depends only on their angular separation on the sky and has a distinctive shape, known as the Hellings and Downs curve (Hellings & Downs, 1983), which we will now derive.

The redshift of the rate of arrival of pulses for a pulsar at a distance L from Earth, in the direction of the unit spatial vector \vec{p} induced by a GW travelling in the direction of the unit vector $\hat{\Omega}$ is given by (Anholm et al., 2009)

$$z(t, \hat{\Omega}) = \frac{1}{2} \frac{\hat{p}^j \hat{p}^i}{1 + \hat{\Omega} \cdot \hat{p}} \left(h_{ij}^{\text{Pulsar}}(t - L, \hat{\Omega}) - h_{ij}^{\text{Earth}}(t, \hat{\Omega}) \right) = \frac{1}{2} \frac{\hat{p}^j \hat{p}^i}{1 + \hat{\Omega} \cdot \hat{p}} \Delta h_{ij}(t, \hat{\Omega}) . \quad (41)$$

The redshift includes two terms, the pulsar term and the Earth term. The pulsar term is often neglected in PTA analysis as it can be considered as an extra noise term which averages to zero. The experimentally measured quantity is not the redshift but the timing residual, the two are related via

$$R(t, \hat{\Omega}) = \int_0^t dt' z(t', \hat{\Omega}) . \quad (42)$$

All of the pulsars, and the Earth, reside in the same metric perturbation field which may be expressed in terms of its Fourier transform

$$h_{ij}(t, \hat{x}) = \sum_{A=+, \times} \int df \iint_{S^2} d\hat{\Omega} \tilde{h}_A(f, \hat{\Omega}) e_{ij}^A(\hat{\Omega}) e^{2\pi i f(t - \hat{\Omega} \cdot \vec{x})}, \quad (43)$$

where $e_{ij}^A(\hat{\Omega})$ is the A polarisation basis tensor for direction $\hat{\Omega}$. Choosing the SSB as the origin of our coordinate system, so the pulsar is at position $L\hat{p}$, gives

$$\Delta h_{ij}(t, \hat{\Omega}) = \sum_{A=+, \times} \int df \tilde{h}_A(f, \hat{\Omega}) e_{ij}^A(\hat{\Omega}) e^{2\pi i f t} \left(e^{-2\pi i f L(1 + \hat{p} \cdot \hat{\Omega})} - 1 \right). \quad (44)$$

From (41) and (44) the Fourier transform of the redshift, $\tilde{z}(f, \hat{\Omega})$, may be read off as

$$\tilde{z}(f, \hat{\Omega}) = \left(e^{-2\pi i f L(1 + \hat{p} \cdot \hat{\Omega})} - 1 \right) \sum_{A=+, \times} \tilde{h}_A(f, \hat{\Omega}) F^A(\hat{\Omega}), \text{ where } F^A(\hat{\Omega}) = \frac{e_{ij}^A(\hat{\Omega}) \hat{p}^j \hat{p}^i}{2(1 + \hat{\Omega} \cdot \hat{p})}. \quad (45)$$

The function $F^A(\hat{\Omega})$ may be regarded as the PTA equivalent of the detector response functions in (38). The stochastic background of GWs is fully characterised by the one-sided power spectral density via the following expectation value

$$\langle h_A^*(f, \hat{\Omega}) h_{A'}(f', \hat{\Omega}') \rangle = \frac{1}{2} S_h(f) \delta^{(2)}(\hat{\Omega}, \hat{\Omega}') \delta_{AA'} \delta(f - f'), \quad (46)$$

where $\delta^{(2)}(\hat{\Omega}, \hat{\Omega}')$ is the delta function on the sphere. From (46) and (45) the expectation of the product of signals from two different pulsars in directions \hat{p}_1 and \hat{p}_2 may be evaluated

$$\begin{aligned} \langle z_1(f) z_2^*(f') \rangle &= \frac{1}{2} S_h(f) \delta(f - f') \Gamma(f) \quad \text{where,} \\ \Gamma(f) &= \sum_{A=+, \times} \iint_{S^2} d\hat{\Omega} \left(e^{2\pi i f L_1(1 + \hat{\Omega} \cdot \hat{p}_1)} - 1 \right) \left(e^{-2\pi i f L_2(1 + \hat{\Omega} \cdot \hat{p}_2)} - 1 \right) F_1^A(\hat{\Omega}) F_2^A(\hat{\Omega}). \end{aligned} \quad (47)$$

The overlap function, $\Gamma(f)$, tends to a constant value in the limit that the distances to the pulsars are large compared to the wavelength of GWs, PTAs operate in this limit, so the overlap may be approximated as a constant

$$\Gamma(f) \approx \Gamma_0 = \sum_{A=+, \times} \iint_{S^2} d\hat{\Omega} F_1^A(\hat{\Omega}) F_2^A(\hat{\Omega}). \quad (48)$$

Neglecting the exponential terms in the overlap is the frequency domain equivalent of neglecting the pulsar term in (41). The integral may be evaluated to give an expression depending only on the angle, θ , between the two pulsars; this is the famous Hellings and Downs curve, see figure 2,

$$\Gamma_0 = \frac{1}{2} + \frac{3x}{2} \left(\log(x) - \frac{1}{6} \right) \quad \text{where } x = \frac{1 - \cos \theta}{2}. \quad (49)$$

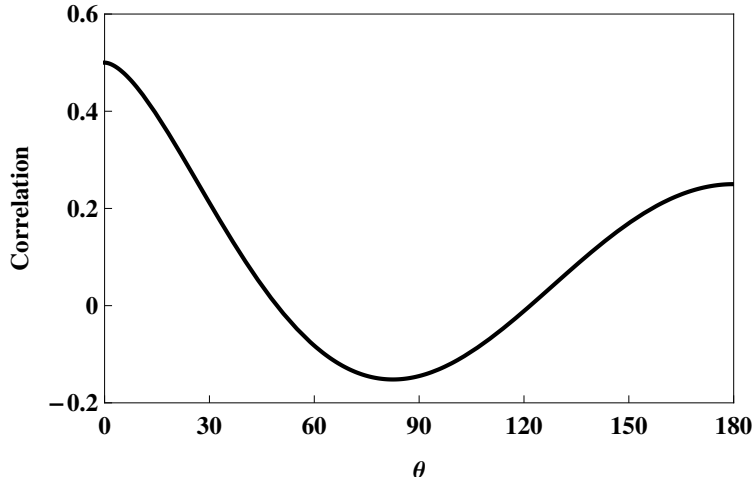


Figure 2: The Hellings and Downs curve, the correlation between two pulsars separated on the sky by an angle θ .

The sensitivity bandwidth of a PTA is set by the sampling properties of the data set. If measurements are spaced in time by δt and taken for a total length of time T then the PTA is sensitive to frequencies in the range $(1/T) < f < (1/\delta t)$. The characteristic strain that the PTA is sensitive to scales linearly with f in this range. This gives the wedge shaped curves plotted in figures A1, A2 and A3. The absolute value of the sensitivity is fixed by normalising to a calculated limit at a given frequency for each PTA. For a discussion of the sensitivities of PTA to both individual sources and stochastic background see Moore et al. (2014).

There is a discrepancy between the treatment of PTA sensitivity curves here and the higher frequency detectors discussed in sections 4.2 and 4.3. When observing a long lived source, such as an inspiral, with a high frequency detector the convention was to define a *characteristic* strain to satisfy (15). Here the convention is to leave the strain untouched and instead adjust the PTA sensitivity curve with observation time, again to satisfy (15). This discrepancy is an unfortunate result of the conventions in use by the different GW communities; however it is also natural given the sources under observation. When observing a transient source, such as a burst or inspiral, which changes within the lifetime of the detector it is natural to consider the detector as performing constantly while the signal changes. However when observing a monochromatic source or a stochastic background which is unchanging over the detector lifetime it is more natural to consider the source as being fixed and the sensitivity of the detector gradually improving. All that is required by the definition in (15) is that the ratio $h_c(f)/h_n(f)$ is constant.

4.4.1. EPTA/PPTA/NANOGrav The PTAs currently in operation are the EPTA (European Pulsar Timing Array), PPTA (Parkes Pulsar Timing Array, based in Australia) and NANOGrav (North American Nanohertz Observatory for GWs). There are published limits on the amplitude of the stochastic background from all three detectors: currently the lowest is from the EPTA, van Haasteren et al. (2011). The EPTA curves in the figures show the published limit based on an analysis of 5 pulsars over approximately 10 years.

4.4.2. IPTA Combining the existing arrays would yield a single PTA using approximately 4 times as many pulsars. The IPTA curves plotted in the figures are based on 20 pulsars timed for twice as long as the current EPTA.

4.4.3. SKA The sensitivity curve plotted in figures A1, A2 and A3 for the SKA (Square Kilometer Array) assume a values of $\delta t_{\text{r.m.s.}}^2$ a factor of 10 better than current PTAs and 20 pulsars timed for twice as long as the current EPTA.

5. Astrophysical sources

All the sources described here are represented by shaded boxes in figures A1, A2 and A3. The boxes are drawn in such a way that there is a reasonable event rate for sources at a detectable SNR. Descriptions of each source are given in the following sections. Sources with short durations and sources which evolve in time over much longer timescales than our observations are drawn with flat topped boxes. Inspiralling binaries, or stochastic backgrounds of binaries, are drawn with a sloping top proportional to $f^{-2/3}$, which is result derived in section 3.2. The width of the box gives the range of frequencies sources of a given type can have a while remaining at a detectable amplitude.

5.1. Sources for ground based detectors

5.1.1. Neutron star binaries The inspiral and merger of a pair of neutron stars is the primary target for ground based detectors. The expected event rate for this type of source is uncertain, but estimates centre around $\rho_{\text{NS-NS}} = 1.3 \times 10^{-4} \text{ Mpc}^{-3}\text{yr}^{-1}$, Abadie et al. (2012b). Plotted in figures A1, A2 and A3 is a box with an amplitude such that it produces a ratio $h_c/h_n = 16$ for advanced LIGO at peak sensitivity and a width between (3 – 300) Hz.

5.1.2. Supernovae Simulations of core collapse supernova events show that GWs between $(10^2 - 10^3) \text{ Hz}$ can be produced. The GW signal undergoes $\mathcal{O}(1)$ oscillation and hence is burst-like. Dimmelmeier et al. (2002) calculate the average maximum amplitude of GWs for a supernova at distance r as

$$h = 8.9 \times 10^{-21} \left(\frac{10 \text{ kpc}}{r} \right). \quad (50)$$

The event rate for supernova is approximately $\rho_{\text{SN}} = 5 \times 10^{-4} \text{ Mpc}^{-3} \text{ yr}^{-1}$. The box plotted in figures A1, A2 and A3 corresponds to a distance $r = 3 \text{ Mpc}$ with the frequency range quoted above. The LIGO and VIRGO detectors have already placed bounds on the event rate for these sources, Abadie et al. (2012a).

5.1.3. Continuous waves from rotating neutron stars If someone is feeling keen they can write a very short section on these, maybe using this reference Aasi et al. (2013). Can whoever writes this section say that in figures A1, A2 and A3 the rotating neutron stars share the same box as supernova.

5.2. Sources for space based detectors

For a review of the GW sources for space based missions see, for example, Amaro-Seoane et al. (2012a), Gair et al. (2012) or the eLISA yellow book (2012).

5.2.1. Massive black hole binaries Space based detectors will be sensitive to equal mass mergers in the range $(10^4 - 10^7) M_{\odot}$. Predictions of the event rate for these mergers range from $\mathcal{O}(3 - 300) \text{ yr}^{-1}$ for LISA with SNRs of up to 10000. The uncertainty in the rate reflects our uncertainty in the growth mechanisms of the supermassive black hole population. Plotted in figures A1, A2 and A3 is a box with a ratio $h_c/h_n = 100$ for eLISA at its peak sensitivity. The range of frequencies plotted is $(3 \times 10^{-4} - 3 \times 10^{-1}) \text{ Hz}$, this corresponds to circular binaries in the mass range quoted above.

5.2.2. Galactic white dwarf binaries These are the most numerous GW sources, they are also the only source where several guaranteed sources have already been indentified by electromagnetic observations, these are known as the verification binaries, Stroeer & Vecchio (2006).

Galactic binaries divide into two classes; the unresolvable and the resolvable galactic binaries. The unresolvable binaries overlap to form a stochastic background as discussed in section 3.2. Plotted in figures A1, A2 and A3 is the estimate of this background due to Nelemans et al. (2001) where an observation time of one year has been assumed

$$h_c(f) = 5 \times 10^{-21} \left(\frac{f}{10^{-3} \text{ Hz}} \right)^{-2/3}. \quad (51)$$

Estimates for the event rate of resolvable binaries centre around $\mathcal{O}(10^3)$ events for eLISA. The box plotted in figures A1, A2 and A3 has an ratio $h_c/h_n = 50$ for eLISA at its peak sensitivity, the frequency range of the box is $(3 \times 10^{-4} - 10^{-2}) \text{ Hz}$, based on visual inspection of Monte Carlo population simulation results presented in Amaro-Seoane et al. (2012a).

5.2.3. Extreme mass ratio inspirals EMRI events occur when a compact stellar mass object inspirals into a supermassive black hole. There is extreme uncertainty in the event rate for EMRIs due to the poorly constrained astrophysics in galactic centres; the best guess estimate is $\mathcal{O}(10)$ events per year with eLISA with $\text{SNR} \geq 20$. The box plotted in figures A1, A2 and A3 has a characteristic strain of $h_c = 3 \times 10^{-20}$ at 10^{-2} Hz which corresponds to a $10M_\odot$ BH inspiralling into a 10^6M_\odot black hole at a luminosity distance of 1 Gpc. The frequency width of the box is somewhat unknown, EMRI events can occur into a black hole of any mass, and hence EMRIs can occur at any frequency. However there is substantial uncertainty in the black hole mass function, so the box in figures A1, A2 and A3 is drawn with a width comparable to that of the LISA sensitivity curve.

5.3. Sources for PTAs

5.3.1. Supermassive black hole binaries The main target for PTAs is a stochastic background of GWs produced by a population of supermassive black hole binaries at cosmological distances. Supermassive black holes are known to lie at the centres of most galaxies and the black hole mergers are associated with the mergers of the host galaxies. The current best published limit for the amplitude of the stochastic background is $h_c = 6 \times 10^{-15}$ at a frequency of $f_0 = 1 \text{ yr}^{-1}$, van Haasteren et al. (2011). There is strong theoretical evidence that the actual background lies close to the current limit, Sesana (2012).

Supermassive black hole binaries at higher frequencies are inspiralling faster and hence there are fewer of them per frequency bin. At a certain frequency, these sources will cease to be a background and become individually resolvable. It is currently unclear whether PTAs will detect an individual binary or a stochastic background first. Plotted in figures A1, A2 and A3 for the unresolvable background is a third of the current limit with a cut off frequency of $f = 1 \text{ yr}^{-1}$ which is suggested by Monte Carlo population studies, Sesana et al. (2008). For the resolvable sources the amplitude of the current limit is plotted between $(3 \times 10^{-9} - 3 \times 10^{-7})$ Hz.

5.4. Cosmological sources

In addition to the sources above, early Universe processes, such as inflation (Grishchuk, 2005) or a first-order phase transition (Binétruy et al., 2012), could have created GWs. More speculatively, it has been hypothesised that cosmic strings could also be a potential source (Damour & Vilenkin, 2005; Binétruy et al., 2012). These relic GWs allow us to explore energy scales far beyond those accessible by other means, providing insight into new and exotic physics. The excitement surrounding the tentative discovery by BICEP2 of the imprint of primordial GWs (generated during inflation) in the cosmic microwave background (Ade et al., 2014), and the subsequent flurry of activity, has shown the scientific potential of such cosmological GWs. These GW signals are so alluring because they probe unknown

physics; this also makes them difficult to predict. Cosmological stochastic backgrounds have been predicted across a range of frequencies with considerable variation in amplitude. As a consequence of this uncertainty, although we could learn much from measuring these signals, we have not included them amongst the sources shown in figures A1, A2 and A3.

6. Concluding remarks

When quantifying the sensitivity of a GW detector and the loudness of a GW source there are three commonly used quantities: the characteristic strain, the power spectral density, and the spectral energy density. Here we have carefully defined these quantities and derived the relationships between them. In addition example sensitivity curve plots using each of these quantities have been presented for a wide range of ground based detectors, space based detectors and pulsar timing arrays. Also plotted are predicted amplitudes for a wide range of sources, these predictions are based on astrophysical estimates of the event rates for a range of processes and are subject to varying degrees of uncertainty. There also exists the exciting possibility of sources nobody has yet considered. Interactive versions of these plots with user specified detectors and sources are made available on-line at <http://www.ast.cam.ac.uk/~rhc26/sources/>. Trying to summarise an entire field of astronomy on one plot is an impossible task; however we hope that the figures and analysis presented here provide useful insight.

Acknowledgments

Christopher Moore is supported by the STFC. I would like to thank Dr Jonathan Gair, Christopher Berry and Robert Cole for help producing this work. I would also like to thank Robert Cole for help producing the figures on the website.

References

- Aasi, J., Abadie, J., Abbott, B. P., et al. 2013, *prd*, 87, 042001
- Abadie, J., Abbott, B. P., Abbott, R., et al. 2012a, *prd*, 85, 122007
- . 2012b, *prd*, 85, 082002
- Abbott, B. P., Abbott, R., Adhikari, R., et al. 2009, *Reports on Progress in Physics*, 72, 076901
- Accadia, T., Acernese, F., Antonucci, F., et al. 2011, *Classical and Quantum Gravity*, 28, 114002
- Accadia, T., Acernese, F., Alshourbagy, M., et al. 2012, *Journal of Instrumentation*, 7, P03012

- Acernese, F., et al. 2009, Advanced Virgo Baseline Design, Virgo Technical Report VIR-0027A-09
- Ade, P. A. R., Aikin, R. W., Barkats, D., et al. 2014, Physical Review Letters, 112, 241101
- Amaro-Seoane, P., Aoudia, S., Babak, S., et al. 2012a, ArXiv e-prints, arXiv:1201.3621
- . 2012b, *cqg*, 29, 124016
- Ando, M., & TAMA Collaboration. 2002, Classical and Quantum Gravity, 19, 1409
- Anholm, M., Ballmer, S., Creighton, J. D. E., Price, L. R., & Siemens, X. 2009, *prd*, 79, 084030
- Binétruy, P., Bohé, A., Caprini, C., & Dufaux, J.-F. 2012, Journal of Cosmology and Astroparticle Physics, 2012, 027
- Chatterji, S., Blackburn, L., Martin, G., & Katsavounidis, E. 2004, Classical and Quantum Gravity, 21, S1809
- Damour, T., & Vilenkin, A. 2005, Physical Review D, 71, 063510
- Dimmelmeier, H., Font, J. A., & Müller, E. 2002, *å*, 393, 523
- eLISA yellow book. 2012, <http://www.elisa-ngo.org/news/news-yellow-book>
- Finn, L. S., & Chernoff, D. F. 1993, *prd*, 47, 2198
- Finn, L. S., & Thorne, K. S. 2000, *prd*, 62, 124021
- Foster, R. S., & Backer, D. C. 1990, *apj*, 361, 300
- Gair, J. R., Vallisneri, M., Larson, S. L., & Baker, J. G. 2012, ArXiv e-prints, arXiv:1212.5575
- Grishchuk, L. P. 2005, Physics-Uspekhi, 48, 1235
- Grote, H., & LIGO Scientific Collaboration. 2008, Classical and Quantum Gravity, 25, 114043
- Harry, G. M., & LIGO Scientific Collaboration. 2010, Classical and Quantum Gravity, 27, 084006
- Hellings, R. W., & Downs, G. S. 1983, *apjl*, 265, L39
- Hild, S., Abernathy, M., Acernese, F., et al. 2011, Classical and Quantum Gravity, 28, 094013
- Jenet, F. A., Hobbs, G. B., van Straten, W., et al. 2006, *apj*, 653, 1571
- Klimenko, S., Yakushin, I., Mercer, A., & Mitselmakher, G. 2008, Classical and Quantum Gravity, 25, 114029
- Misner, C. W., Thorne, K. S., & Wheeler, J. A. 1973, Gravitation
- Moore, C. J., Taylor, S. R., & Gair, J. R. 2014, ArXiv e-prints, arXiv:1406.5199
- Nelemans, G., Yungelson, L. R., & Portegies Zwart, S. F. 2001, Astron. Astrophys., 375, 890
- Ott, C. D. 2009, Classical and Quantum Gravity, 26, 063001

- Peters, P. C., & Mathews, J. 1963, Physical Review, 131, 435
- Sathyaprakash, B. S., & Schutz, B. F. 2009, Living Reviews in Relativity, 12, 2
- Sesana, A. 2012, ArXiv e-prints, arXiv:1211.5375
- Sesana, A., Vecchio, A., & Colacino, C. N. 2008, mn, 390, 192
- Somiya, K. 2012, Classical and Quantum Gravity, 29, 124007
- Stroeer, A., & Vecchio, A. 2006, Classical and Quantum Gravity, 23, 809
- van Haasteren, R., Levin, Y., Janssen, G. H., et al. 2011, mn, 414, 3117
- Yagi, K., & Seto, N. 2011, prd, 83, 044011

Appendix A. Sensitivity curves

The plots in this section show all of the detectors and sources described in the text. Interactive versions of these plots may be viewed on-line, <http://www.ast.cam.ac.uk/~rhc26/sources/>. The detector noise curves all have their resonance spikes removed for clarity.

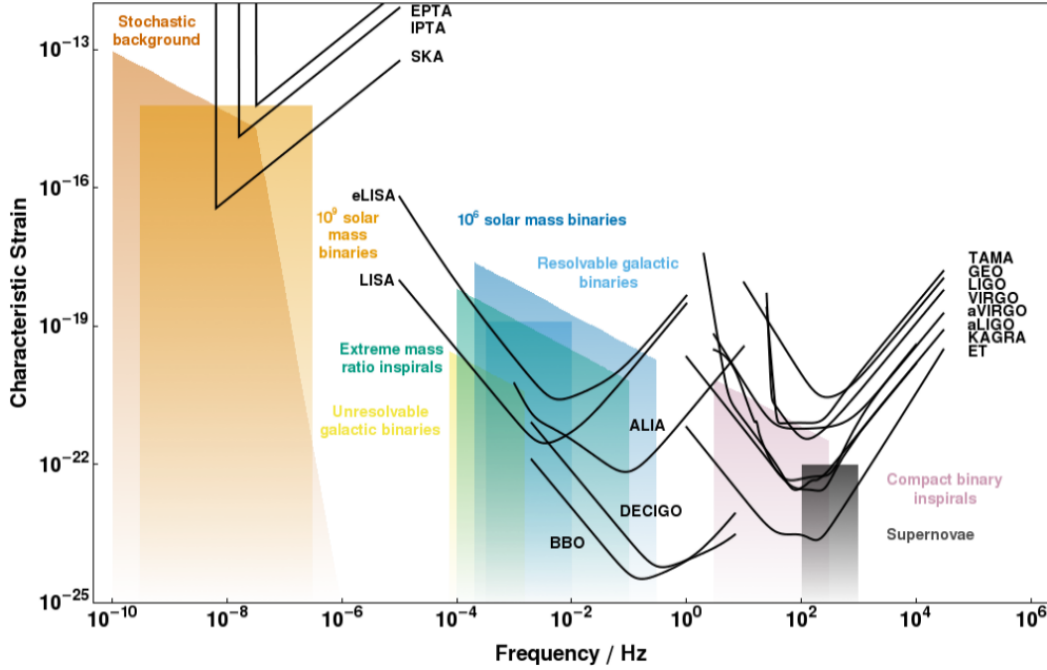


Figure A1: A plot of characteristic strain against frequency for a variety of detectors and sources.

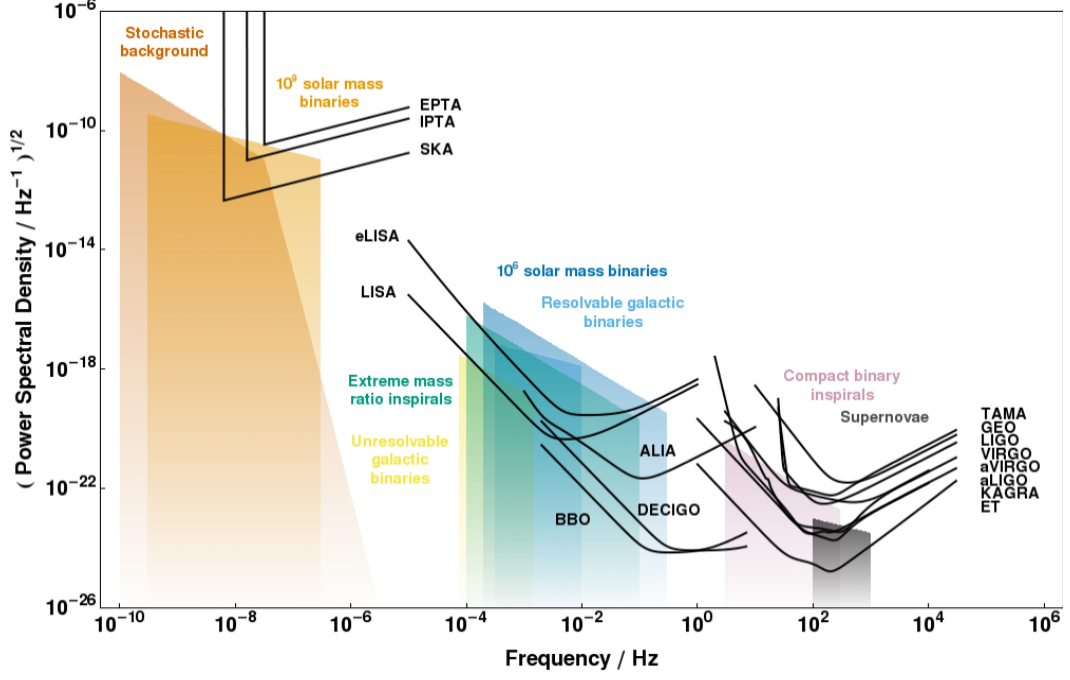


Figure A2: A plot of the square root of power spectral density against frequency for a variety of detectors and sources.

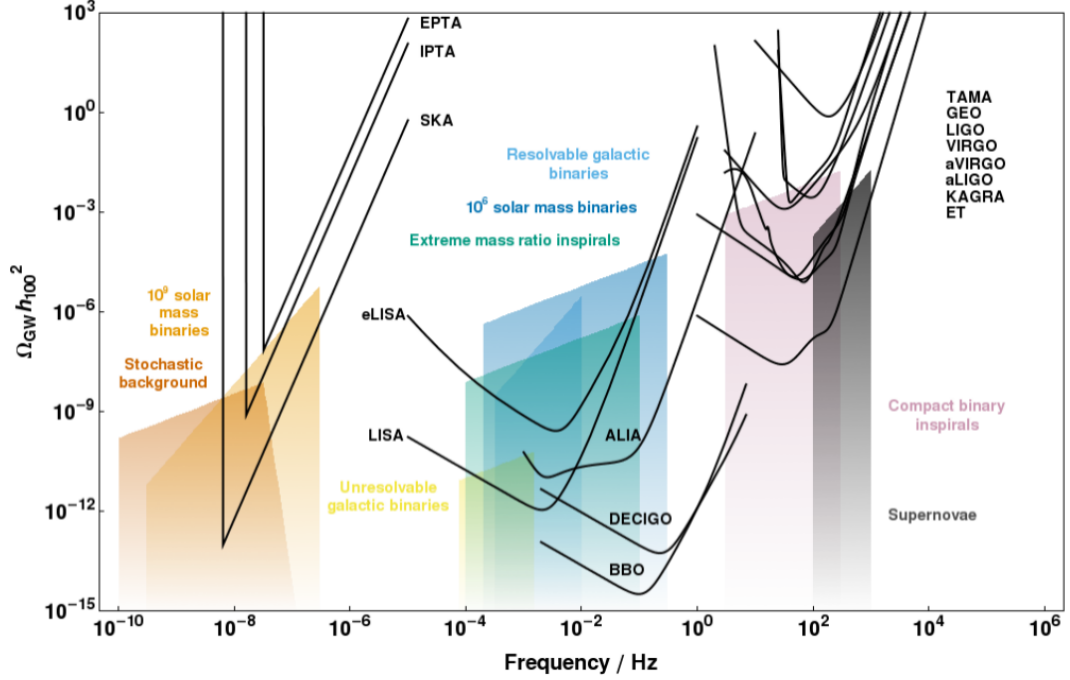


Figure A3: A plot of the dimensionless energy density in GWs against frequency for a variety of detectors and sources.